Mode and Polarization Selective Pressure and Shear Wave Scattering by Grouting Defects in Tendon Ducts

Alexander ZIMMER, K.J. LANGENBERG, Dept. Electrical Engineering and Computer Science University of Kassel, Kassel, Germany

Abstract We propose a novel algorithm to calculate images of defects, which is based on the physical properties of elastic wave modes being either curl-free pressure or divergence-free shear waves; the mode and polarization selection is performed in the spatial Fourier domain, where it can be combined with Fourier based frequency diversity diffraction tomography.

1. Introduction

Elastic waves in solids exist as primary pressure and secondary shear waves reflecting their respective wave speeds and physical properties: pressure waves are curl-free and shear waves are divergence-free. Appropriate algorithmic exploitation for a separation of wave modes and polarization to extract specific information about a scatterer (i.e. a grouting defect in a tendon duct) would therefore consist in the calculation of the curl and divergence of the displacement vector of a scattered wave field. Yet, this would require the knowledge of the field in a spatial volume, and usually the only available access to the field is on the surface of a part. If this surface is planar, a two-dimensional spatial Fourier transform with regard to cartesian scan coordinates can be performed, reducing the curl and the divergence operations to cross- and dot-multiplications with an appropriately defined Fourier vector. Combination of this pre-processing with an imaging algorithm which is equally based on spatially Fourier transformed data (FT-SAFT for Fourier Transform Synthetic Aperture Focusing Technique: [1,2]) results in a mode and polarization selective elastodynamic vector diffraction tomography yielding complementary information in defect images. Here, we will present the underlying equations and demonstrate the principle of the method for two-dimensional synthetic data calculated in terms of eigenfunction expansions of the scattered wave field of a circular cylindrical as a simple model for a tendon duct in concrete.

2. Plane Wave Scattering by Circular Cylinders

The two-dimensional elastodynamic scattering problem decouples into a strictly scalar shear horizontal (SH) and a vector pressure-shear-vertical (P-SV) problem, which involves mode conversion. Aiming at mode and polarization selective imaging we concentrate on the second one. Let us consider a circular cylinder of radius a with a traction-free boundary S_c with outward normal $\underline{\mathbf{n}}_c$ embedded in a homogeneous isotropic material with density ρ

and forth rank stiffness tensor $\underline{\underline{\underline{\underline{\mathbf{c}}}}}$, which, for isotropic materials, contains only Lamé constants λ and μ as entries resulting in pressure and shear wave speeds $c_{\mathrm{P}} = \sqrt{(\lambda + 2\mu)/\rho}$ and $c_{\mathrm{S}} = \sqrt{\mu/\rho}$, respectively (Fig. 1); the two-dimensional vector of position is denoted by $\underline{\mathbf{r}}$ making an angle θ with the z-axis. An incident impulsive plane longitudinally polarized P-wave — the unit-vector $\hat{\underline{\mathbf{u}}}_{i\mathrm{P}}$ denoting the polarization vector — or a plane transversely polarized SV-wave with polarization vector $\hat{\underline{\mathbf{u}}}_{i\mathrm{SV}}$ and propagation direction $\hat{\underline{\mathbf{k}}}_i$ yields a P-SV-coupled scattered field in terms of the particle displacement vector $\underline{\mathbf{u}}(\underline{\mathbf{r}},t)$ as function of space and time t.

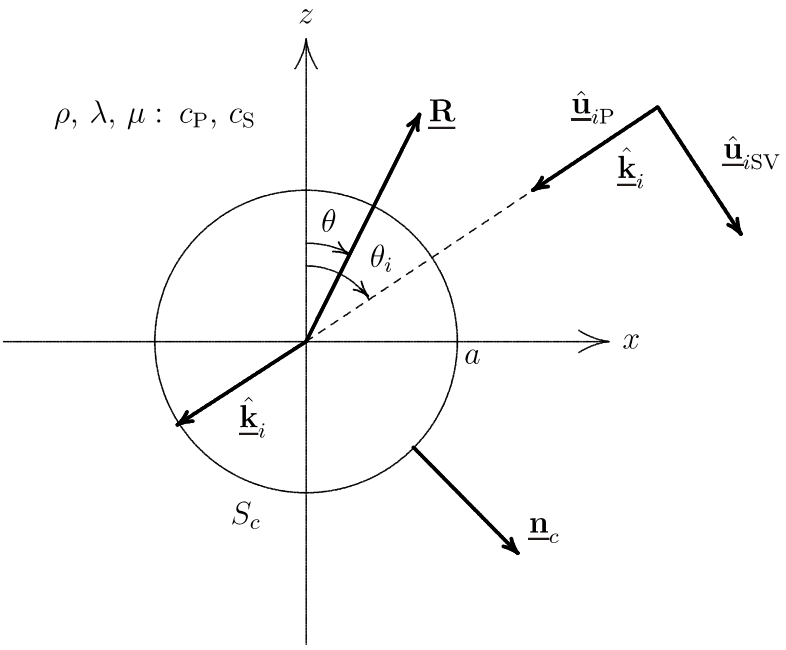

Figure 1. Scattering of a plane P- or SV-wave by a circular cylinder with a traction-free surface

As mentioned in the introduction, $\underline{\mathbf{u}}(\underline{\mathbf{r}},t)$ can be separated into a P-term being derived from the gradient $\nabla\Phi(\underline{\mathbf{r}},t)$ of a scalar (Helmholtz) potential $\Phi(\underline{\mathbf{r}},t)$ and an SV-curl-term $\nabla\times\Psi_y(\underline{\mathbf{r}},t)\underline{\mathbf{e}}_y$ of a vector potential $\Psi_y(\underline{\mathbf{r}},t)\underline{\mathbf{e}}_y$ — $\underline{\mathbf{e}}_y$ being the unit-vector in y-direction — according to

$$\underline{\mathbf{u}}(\underline{\mathbf{r}},t) = \nabla\Phi(\underline{\mathbf{r}},t) + \nabla\times\Psi_y(\underline{\mathbf{r}},t)\underline{\mathbf{e}}_y \quad . \tag{2.1}$$

Switching from time to (circular) frequency ω by means of a Fourier transform, the correspondingly transformed potentials satisfy Helmholtz equations with wave numbers $k_{\mathrm{P,S}} = \omega/c_{\mathrm{P,S}}$:

$$\Delta\Phi(\underline{\mathbf{r}},\omega) + k_{\mathrm{P}}^2\Phi(\underline{\mathbf{r}},\omega) = 0 \quad , \tag{2.2}$$

$$\Delta\Psi_y(\underline{\mathbf{r}},\omega) + k_{\mathrm{S}}^2\Psi_y(\underline{\mathbf{r}},\omega) = 0 \tag{2.3}$$

whose solutions are given as the superposition of the potentials of the selected incident wave

$$\Phi_i(\underline{\mathbf{r}},\omega,\hat{\underline{\mathbf{k}}}_i) = \phi_i(\omega)\,\mathrm{e}^{\,\mathrm{j}k_\mathrm{P}\hat{\underline{\mathbf{k}}}_i\cdot\underline{\mathbf{r}}} \quad , \tag{2.4}$$

$$\Psi_{iy}(\underline{\mathbf{r}},\omega,\hat{\underline{\mathbf{k}}}_i) = \psi_i(\omega)\,\mathrm{e}^{\,\mathrm{j}k_\mathrm{S}\hat{\underline{\mathbf{k}}}_i\cdot\underline{\mathbf{r}}} \tag{2.5}$$

with the corresponding spectra $\phi_i(\omega)$, $\psi_i(\omega)$ of the chosen impulse, and the scattered wave potentials as eigenfunction expansions in cylindrical coordinates

$$\Phi_s(r,\theta,\omega) = \sum_{n=-\infty}^{\infty} \phi_n(\omega)\mathrm{H}_n^{(1)}(k_\mathrm{P}r)\,\mathrm{e}^{\,\mathrm{j}n\theta} \quad , \tag{2.6}$$

$$\Psi_{sy}(r,\theta,\omega) = \sum_{n=-\infty}^{\infty} \psi_n(\omega)\mathrm{H}_n^{(1)}(k_\mathrm{S}r)\,\mathrm{e}^{\,\mathrm{j}n\theta} \tag{2.7}$$

implying Hankel functions $\mathrm{H}_n^{(1)}(k_{\mathrm{P,S}}r)$ of the first kind and order n; r is the magnitude of $\underline{\mathbf{r}}$. The expansion coefficients $\phi_n(\omega)$ and $\psi_n(\omega)$ are determined imposing the stress-free boundary condition on the resulting displacement vector with the knowledge of the pertinent expansion of the incident plane wave. Assuming a "measurement" surface (or line) at a distance $z = d > a$, the cartesian components of $u_x(x,d,t)$, $u_z(x,d,t)$ can be computed as function of x from (2.1) with (2.6) and (2.7) after an inverse Fourier transform with respect to ω. Fig. 2 shows the resulting xt-data (B-scan data) for an incident P- and Fig. 3 for an incident SV-wave with $\hat{\underline{\mathbf{k}}}_i = -\underline{\mathbf{e}}_z$ and time dependence according to two cycles of a time harmonic pulse with a raised cosine amplitude modulation, which represents a suitable approximation of a transducer pulse. Typically, each displacement exhibits pressure and shear wave diffraction curves as being recognized by the different slopes.

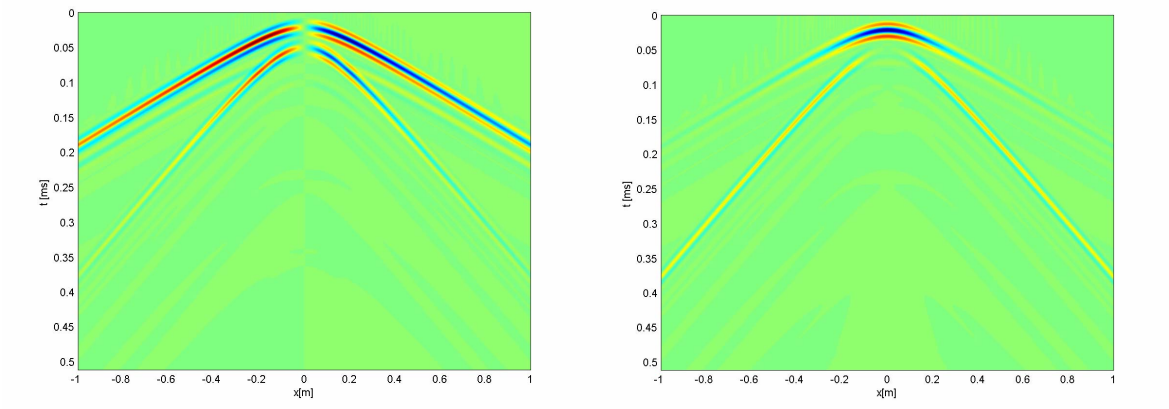

Figure 2. B-scan pressure and shear diffraction curves for P-wave incidence (left: x-component; right: z-component)

The case of SV-incidence additionally shows the strongly excited shear creeping wave traveling around the cylinder. Hence, imaging algorithms relying on pressure or shear wave speed backpropagation like SAFT [1] can only be applied after mode and polarization selection.

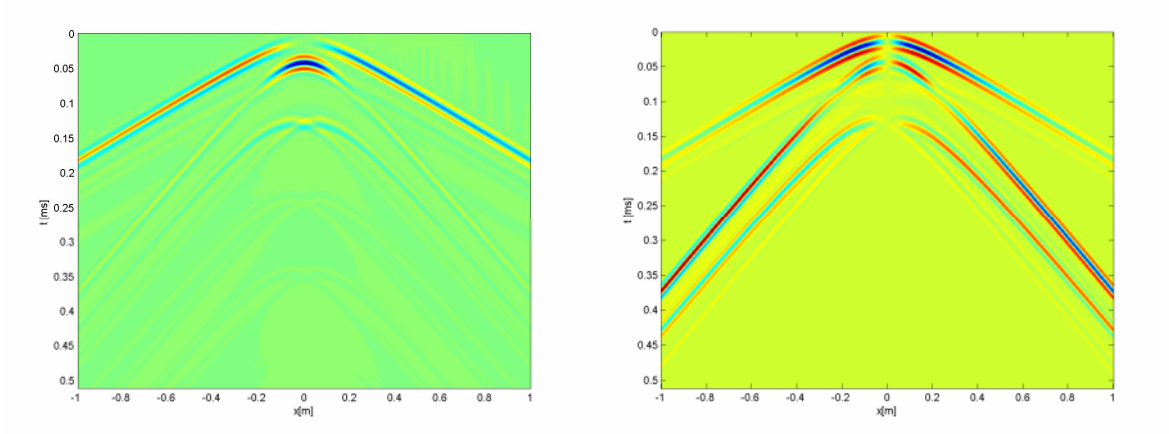

Figure 3. B-scan pressure and shear diffraction curves for SV-wave incidence (left: x -component; right: z -component)

3. Mode and Polarization Selective Elastodynamic Imaging

Proper defect imaging from recorded data should be formulated as an inverse scattering problem requiring an appropriate mathematical representation of the scattered field bound for inversion. Since we finally apply the resulting algorithms to three-dimensional problems, i.e. two-dimensional scan-data, we start with the three-dimensional representation integral [3]

$$\underline{\mathbf{v}}(\underline{\mathbf{R}},\omega) = \iiint_{V_Q} \left[-\mathrm{j}\omega \underline{\mathbf{f}}(\underline{\mathbf{R}}',\omega) \cdot \underline{\underline{\Gamma}}(\underline{\mathbf{R}}-\underline{\mathbf{R}}',\omega) - \underline{\underline{\mathbf{h}}}(\underline{\mathbf{R}}',\omega) : \underline{\underline{\underline{\mathbf{c}}}} : \nabla' \underline{\underline{\Gamma}}(\underline{\mathbf{R}}-\underline{\mathbf{R}}',\omega) \right] \mathrm{d}^3\underline{\mathbf{R}}' \quad (3.1)$$

of the frequency spectrum of the particle velocity vector $\underline{\mathbf{v}}(\underline{\mathbf{R}},\omega)$ as a function of the vector of position $\underline{\mathbf{R}}$ in terms of a point source synthesis involving a dyadic Green function $\underline{\underline{\Gamma}}(\underline{\mathbf{R}}-\underline{\mathbf{R}}',\omega)$ according to

$$\underline{\underline{\Gamma}}(\underline{\mathbf{R}}-\underline{\mathbf{R}}',\omega) = -\frac{1}{\lambda+2\mu}\frac{1}{k_\mathrm{P}^2}\nabla'\nabla'\frac{\mathrm{e}^{\mathrm{j}k_\mathrm{P}|\underline{\mathbf{R}}-\underline{\mathbf{R}}'|}}{4\pi|\underline{\mathbf{R}}-\underline{\mathbf{R}}'|} + \frac{1}{\mu}\left(\underline{\underline{\mathbf{I}}} + \frac{1}{k_\mathrm{S}^2}\nabla'\nabla'\right)\frac{\mathrm{e}^{\mathrm{j}k_\mathrm{S}|\underline{\mathbf{R}}-\underline{\mathbf{R}}'|}}{4\pi|\underline{\mathbf{R}}-\underline{\mathbf{R}}'|} \quad ; \quad (3.2)$$

$\underline{\underline{\mathbf{I}}}$ denotes the dyadic idemfactor, and

$$G_{\mathrm{P,S}}(\underline{\mathbf{R}}-\underline{\mathbf{R}}',\omega) = \frac{\mathrm{e}^{\mathrm{j}k_{\mathrm{P,S}}|\underline{\mathbf{R}}-\underline{\mathbf{R}}'|}}{4\pi|\underline{\mathbf{R}}-\underline{\mathbf{R}}'|} \quad (3.3)$$

is the frequency domain three-dimensional scalar Green function accounting for the two wave speeds of spherical pressure and shear waves. As such, $\underline{\underline{\Gamma}}(\underline{\mathbf{R}}-\underline{\mathbf{R}}',\omega)$ includes the directional dependence of the amplitudes of elementary spherical pressure and shear waves emanating from each single source point within the given sources $\underline{\mathbf{f}}(\underline{\mathbf{R}}',\omega)$ — the force density — and $\underline{\underline{\mathbf{h}}}(\underline{\mathbf{R}}',\omega)$ — the given second rank deformation rate tensor, both being eventually non-zero within a source volume V_Q. With given, prescribed or primary sources inserted into (3.1) this integral describes an incident "transducer" field; if it should describe a scattered field, the given sources have to be replaced by secondary or induced sources,

which are equivalent to the scatterer, i.e. the source integral turns into an equivalence theorem. These equivalent sources differ for penetrable scatterers and scatterers with perfect boundary conditions, i.e. non-penetrable scatterers with, for instance, boundaries free of surface tractions. The derivation of pertinent imaging algorithms always follows the same guidelines, yet it is most intuitive if we assume a penetrable scatterer, which differs from the embedding material only in the mass density yielding a mass density contrast

$$\chi_\rho(\underline{\mathbf{R}}) = \frac{1}{\rho}\left[\rho(\underline{\mathbf{R}}) - \rho\right]\Gamma_c(\underline{\mathbf{R}}) \quad , \tag{3.4}$$

where $\Gamma_c(\underline{\mathbf{R}})$ according to

$$\Gamma_c(\underline{\mathbf{R}}) = \begin{cases} 0 & \text{for } \underline{\mathbf{R}} \notin V_c \\ 1 & \text{for } \underline{\mathbf{R}} \in V_c \end{cases} \tag{3.5}$$

represents the geometry of the scattering volume as its characteristic function. The contrast defines a secondary equivalent force density

$$\underline{\mathbf{f}}_\rho(\underline{\mathbf{R}}, \omega) = -\mathrm{j}\omega\rho\,\chi_\rho(\underline{\mathbf{R}})\underline{\mathbf{v}}(\underline{\mathbf{R}}, \omega) \quad , \tag{3.6}$$

which is obviously dependent on the total particle velocity — the superposition of the incident and the scattered velocity — inside the scattering volume rendering the inverse scattering problem a non-linear problem. Yet the theory of scalar inversion [4] and its application to real-life data [5,2,6] tells us that a linearization is most often appropriate; here, it amounts to the Born approximation replacing the total field in (3.6) by the incident field alone. Assuming the incident wave to be either a plane pressure or a plane shear wave according to

$$\underline{\mathbf{v}}_i^{\mathrm{P,S}}(\underline{\mathbf{R}}, \omega) = v_{\mathrm{P,S}}(\omega)\,\mathrm{e}^{\,\mathrm{j}\underline{\mathbf{k}}_i^{\mathrm{P,S}}\cdot\underline{\mathbf{R}}}\,\hat{\underline{\mathbf{v}}}_{\mathrm{P,S}} \tag{3.7}$$

with phase vectors $\underline{\mathbf{k}}_i^{\mathrm{P,S}} = k_{\mathrm{P,S}}\hat{\underline{\mathbf{k}}}_i^{\mathrm{P,S}}$ and polarizations $\hat{\underline{\mathbf{v}}}_{\mathrm{P}} = \hat{\underline{\mathbf{k}}}_{\mathrm{P}}$ and $\hat{\underline{\mathbf{v}}}_{\mathrm{S}} \times \hat{\underline{\mathbf{k}}}_{\mathrm{S}} = \underline{0}$ we obtain from (3.1) within the Born approximation

$$\underline{\mathbf{v}}_s^{\mathrm{Born}}(\underline{\mathbf{R}}, \omega) = -\omega^2\rho v_{\mathrm{P,S}}(\omega)\hat{\underline{\mathbf{v}}}_{\mathrm{P,S}} \cdot \iiint_{V_c} \chi_\rho(\underline{\mathbf{R}}')\,\mathrm{e}^{\,\mathrm{j}\underline{\mathbf{k}}_i^{\mathrm{P,S}}\cdot\underline{\mathbf{R}}'}\,\underline{\underline{\Gamma}}(\underline{\mathbf{R}} - \underline{\mathbf{R}}', \omega)\,\mathrm{d}^3\underline{\mathbf{R}}' \quad . \tag{3.8}$$

For either pressure or shear wave incidence the two terms in $\underline{\underline{\Gamma}}(\underline{\mathbf{R}} - \underline{\mathbf{R}}', \omega)$ ensure that all (cartesian) components of the scattered field contain both pressure and shear waves (compare Figures 2 and 3). Since we aim at mode and polarization selective imaging we have to suppress either one of these terms algorithmically. As we already pointed out this can be achieved in the spatial Fourier space. With the knowledge of

$$\begin{aligned} \hat{G}(K_x, K_y, d - z', \omega) &= \int_{-\infty}^{\infty}\int_{-\infty}^{\infty} G(x, y, d - z')\,\mathrm{e}^{\,-\mathrm{j}K_x x - \mathrm{j}K_y y}\,\mathrm{d}x\mathrm{d}y \\ &= \frac{\mathrm{j}}{2\sqrt{k^2 - K_x^2 - K_y^2}}\,\mathrm{e}^{\,\mathrm{j}|d-z'|\sqrt{k^2 - K_x^2 - K_y^2}} \end{aligned} \tag{3.9}$$

as the two-dimensional Fourier transform of the scalar Green function with respect to the scan coordinates x and y on the measurement plane at $z = d > z'$ — K_x and K_y denoting

the pertinent Fourier variables — and the definition of the z-component of a Fourier vector $\underline{\mathbf{K}}_{P,S}$ according to

$$\underline{\mathbf{K}}_{\mathrm{P,S}} = K_x \underline{\mathbf{e}}_x + K_y \underline{\mathbf{e}}_y + K_{\mathrm{P,S}z} \underline{\mathbf{e}}_z \quad , \tag{3.10}$$

$$K_{\mathrm{P,S}z} = \sqrt{k_{\mathrm{P,S}}^2 - (K_x + k_{ix}^{\mathrm{P,S}})^2 - (K_y + k_{iz}^{\mathrm{P,S}})^2} - k_{iz}^{\mathrm{P,S}} \tag{3.11}$$

we can relate the two-dimensional Fourier transform of the particle velocity vector (within the Born approximation) to the three-dimensional spatial Fourier transform (indicated by a tilde) of the contrast function for those points in Fourier space satisfying (3.11) [1,6]; yet the ambiguity whether we choose $K_{\mathrm{P}z}$ or $K_{\mathrm{S}z}$ still prevents an explicit scheme. The remedy consists in the pre-processing via dot-multiplication of the Fourier transformed particle velocity with $\underline{\mathbf{K}}_{\mathrm{S}}$ to select the P-mode in the scattered field or via cross-multiplication with $\underline{\mathbf{K}}_{\mathrm{P}}$ to select the two orthogonal polarizations of the S-mode. This exploits the physical nature of pressure and shear waves being curl- or divergence-free, respectively. The detailed derivation then yields the following mode- and polarization selective inversion equations [6] to produce a P-image from P-wave incidence

$$\begin{aligned}&(\underline{\mathbf{K}}_{\mathrm{S}} + \underline{\mathbf{k}}_i^{\mathrm{P}}) \cdot \hat{\underline{\mathbf{v}}}_s^{\mathrm{Born,P}}(K_x + k_{ix}^{\mathrm{P}}, K_y + k_{iy}^{\mathrm{P}}, d, \omega, \hat{\underline{\mathbf{v}}}_{\mathrm{P}}) = \\ &v_{\mathrm{P}}(\omega) \frac{\mathrm{j}}{2(K_{\mathrm{P}z} + k_{iz}^{\mathrm{P}})^2} \mathrm{e}^{\mathrm{j}d(K_{\mathrm{P}z} + k_{iz}^{\mathrm{P}})} (\underline{\mathbf{K}}_{\mathrm{S}} + \underline{\mathbf{k}}_i^{\mathrm{P}}) \cdot (\underline{\mathbf{K}}_{\mathrm{P}} + \underline{\mathbf{k}}_i^{\mathrm{P}})(\underline{\mathbf{K}}_{\mathrm{P}} + \underline{\mathbf{k}}_i^{\mathrm{P}}) \cdot \hat{\underline{\mathbf{v}}}_{\mathrm{P}} \tilde{\chi}_\rho(\underline{\mathbf{K}}_{\mathrm{P}})\end{aligned} \tag{3.12}$$

or a (mode-converted) P-image from S-wave incidence

$$\begin{aligned}&(\underline{\mathbf{K}}_{\mathrm{S}} + \underline{\mathbf{k}}_i^{\mathrm{S}}) \cdot \hat{\underline{\mathbf{v}}}_s^{\mathrm{Born,P}}(K_x + k_{ix}^{\mathrm{S}}, K_y + k_{iy}^{\mathrm{S}}, d, \omega, \underline{\mathbf{v}}_{\mathrm{S}}) \cdot \hat{\underline{\mathbf{v}}}_{\mathrm{S}} = \\ &v_{\mathrm{S}}(\omega) \frac{\mathrm{j}}{2(K_{\mathrm{P}z} + k_{iz}^{\mathrm{S}})^2} \mathrm{e}^{\mathrm{j}d(K_{\mathrm{P}z} + k_{iz}^{\mathrm{S}})} (\underline{\mathbf{K}}_{\mathrm{S}} + \underline{\mathbf{k}}_i^{\mathrm{S}}) \cdot (\underline{\mathbf{K}}_{\mathrm{P}} + \underline{\mathbf{k}}_i^{\mathrm{S}})(\underline{\mathbf{K}}_{\mathrm{P}} + \underline{\mathbf{k}}_i^{\mathrm{S}}) \cdot \hat{\underline{\mathbf{v}}}_{\mathrm{S}} \tilde{\chi}_\rho(\underline{\mathbf{K}}_{\mathrm{P}}) \quad ;\end{aligned} \tag{3.13}$$

similarly an S-image from S-wave incidence

$$\begin{aligned}&(\underline{\mathbf{K}}_{\mathrm{P}} + K_i^{\mathrm{S}}) \times \hat{\underline{\mathbf{v}}}_s^{\mathrm{Born,S}}(K_x + k_{ix}^{\mathrm{S}}, K_y + k_{iy}^{\mathrm{S}}, d, \omega, \hat{\underline{\mathbf{v}}}_{\mathrm{S}}) \cdot \hat{\underline{\mathbf{v}}}_{\mathrm{S}} = \\ &-k_{\mathrm{S}}^2 v_{\mathrm{S}}(\omega) \frac{\mathrm{j}}{2(K_{\mathrm{S}z} + k_{iz}^{\mathrm{S}})^2} \mathrm{e}^{\mathrm{j}d(K_{\mathrm{S}z} + k_{iz}^{\mathrm{S}})} (\underline{\mathbf{K}}_{\mathrm{P}} + \underline{\mathbf{k}}_i^{\mathrm{S}}) \times \left[\underline{\underline{\mathbf{I}}} - \frac{1}{k_{\mathrm{S}}^2} (\underline{\mathbf{K}}_{\mathrm{S}} + \underline{\mathbf{k}}_i^{\mathrm{S}})(\underline{\mathbf{K}}_{\mathrm{S}} + \underline{\mathbf{k}}_i^{\mathrm{S}}) \right] \cdot \hat{\underline{\mathbf{v}}}_{\mathrm{S}} \tilde{\chi}_\rho(\underline{\mathbf{K}}_{\mathrm{S}})\end{aligned} \tag{3.14}$$

and a (mode-converted) S-image from P-wave incidence

$$\begin{aligned}&(\underline{\mathbf{K}}_{\mathrm{P}} + \underline{\mathbf{k}}_i^{\mathrm{P}}) \times \hat{\underline{\mathbf{v}}}_s^{\mathrm{Born,S}}(K_x + k_{ix}^{\mathrm{P}}, K_y + k_{iy}^{\mathrm{P}}, d, \omega, \hat{\underline{\mathbf{v}}}_{\mathrm{P}}) = \\ &-k_{\mathrm{S}}^2 v_{\mathrm{P}}(\omega) \frac{\mathrm{j}}{2(K_{\mathrm{S}z} + k_{iz}^{\mathrm{P}})^2} \mathrm{e}^{\mathrm{j}d(K_{\mathrm{S}z} + k_{iz}^{\mathrm{P}})} (\underline{\mathbf{k}}_{\mathrm{P}} + \underline{\mathbf{k}}_i^{\mathrm{P}}) \times \hat{\underline{\mathbf{v}}}_{\mathrm{P}} \cdot \left[\underline{\underline{\mathbf{I}}} - \frac{1}{k_{\mathrm{S}}^2} (\underline{\mathbf{K}}_{\mathrm{S}} + \underline{\mathbf{k}}_i^{\mathrm{P}})(\underline{\mathbf{K}}_{\mathrm{S}} + \underline{\mathbf{k}}_i^{\mathrm{P}}) \right] \cdot \hat{\underline{\mathbf{v}}}_{\mathrm{P}} \tilde{\chi}_\rho(\underline{\mathbf{K}}_{\mathrm{S}})\end{aligned} \tag{3.15}$$

can be obtained; $\underline{\mathbf{k}}_{i\mathrm{P,S}}$ refers to the incident wave and $\underline{\mathbf{K}}_{\mathrm{P,S}}$, $\underline{\mathbf{v}}^{\mathrm{Born,P,S}}$ to the wave mode to be selected. Obviously, as indicated by the argument of $\tilde{\chi}_\rho$, images obtained with the selected wave mode contain different (complementary) information about the defect. To demonstrate the single steps in this procedure we refer to our two-dimensional numerical example of the circular cylinder; in that case we simply have to put $K_y = 0$ in the above equations. The first thing that we have to check is whether the mode selection works properly, and indeed, this is confirmed by Figures 4 and 5, where the left-hand sides of

(3.12)–(3.15) are displayed after Fourier inversion with regard to frequency and with regard to K_x, i.e. we return to the space-time domain to find separated pressure and shear diffraction curves (note: in the two-dimensional case, the cross-products in (3.13) and (3.14) yield only an $\underline{\mathbf{e}}_y$-component).

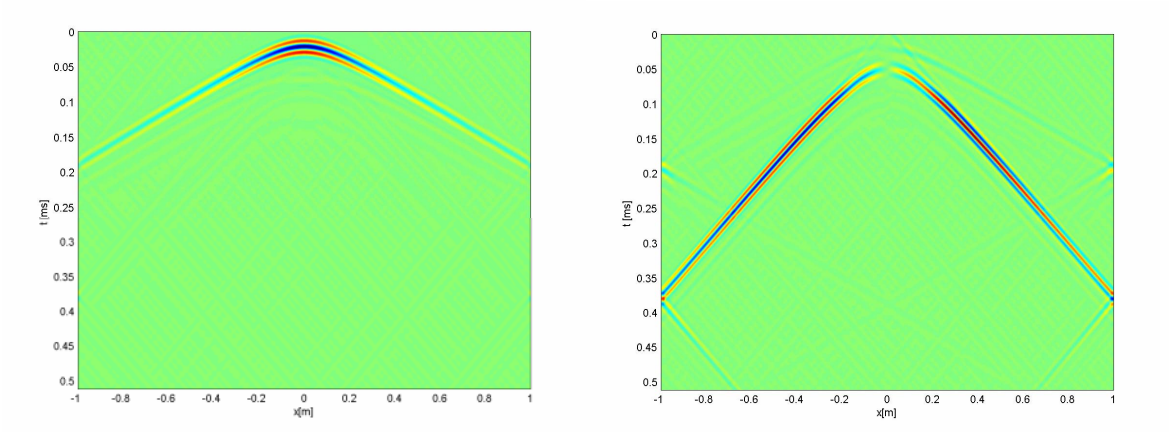

Figure 4. Mode separated P- (left) and SV-diffraction curves (right) for P-wave incidence

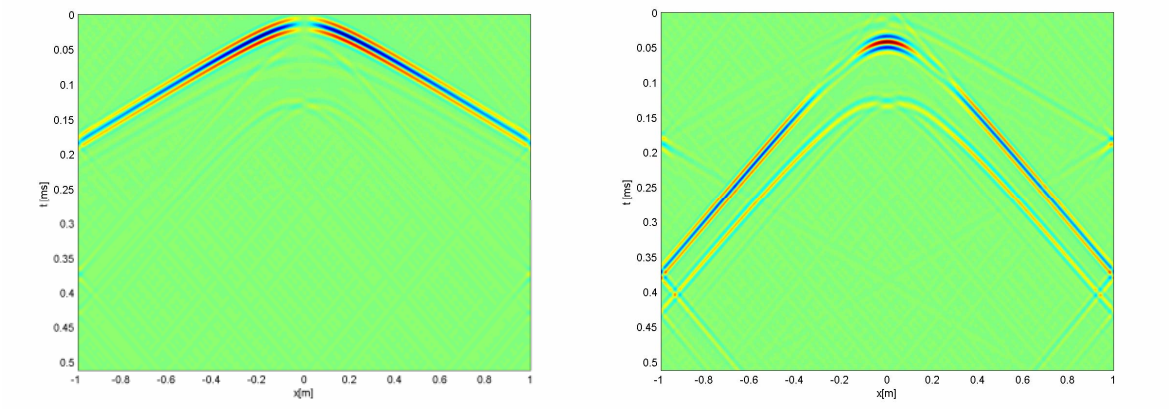

Figure 5. Mode separated SV- (left) and P-diffraction curves (right) for SV-wave incidence

4. Conclusion

The first step in the application of our novel mode and polarization selective imaging algorithms has been illustrated using two-dimensional scattering data from a traction-free cylinder. The next step will certainly be the inversion, namely the complete evaluation of equations (3.12)–(3.15) in a frequency diversity operational mode, i.e. for pulsed excitation. Thereafter, the schemes should be applied to three-dimensional data, which, for a spherical scatterer, can be equally calculated by means of eigenfunction expansions, and for real-life models of grouting defects in tendon ducts with the numerical EFIT-code (Elastodynamic Finite Integration Technique) [7]. Note: Our previously published algorithms referring to the present subject [8] also exploit mode and polarization selection, yet they exert the far-field representation of scattered data and are therefore not equally straightforward.

References

[1] K. Mayer, R. Marklein, K.J. Langenberg and T. Kreutter: Three-dimensional imaging system based on the Fourier transform synthetic aperture technique. Ultrasonics 28 (1990) 241

[2] R. Marklein, K. Mayer, R. Hannemann, T. Krylow, K. Balasubramanian, K.J. Langenberg and V. Schmitz: Linear and nonlinear inversion algorithms applied in nondestructive evaluation. Inverse Problems 18 (2002) 173

[3] A.T. de Hoop: *Handbook of Radiation and Scattering of Waves*. Academic Press, London 1995

[4] K.J. Langenberg: Linear scalar inverse scattering. In: *Scattering and Inverse Scattering in Pure and Applied Science*. Eds.: R. Pike and P.C. Sabatier. Academic Press, London 2002

[5] K.J. Langenberg, M. Brandfaß, R. Hannemann, C. Hofmann, T. Kaczorowski, J. Kostka, R. Marklein, K. Mayer and A. Pitsch: Inverse scattering with acoustic, electromagnetic and elastic waves as applied in nondestructive evaluation. In: *Wavefield Inversion*. Ed.: A. Wirgin. Springer, Vienna 1999

[6] K.J. Langenberg, K. Mayer and R. Marklein: Nondestructive testing of concrete with electromagnetic and elastic waves: Modeling and imaging. Cement & Concrete Composites 28 (2006) 370

[7] R. Marklein: The Finite Integration Technique as a general tool to compute acoustic, electromagnetic, elastodynamic and coupled wave fields. In: *Review of Radio Science 1999–2002*. Ed.: W.R. Stone. IEEE Press, Piscataway 2002

[8] J. Kostka, K.J. Langenberg, K. Mayer and M. Krause: Improved flaw imaging applying elastodynamic far-field Fourier inversion (EL-FT-SAFT). Proc. 2nd Int. Conf. on Computer Methods and Inverse Problems in Nondestructive Testing and Diagnostics (Minsk, October 1998) 397